Quantum spin Hall effect and topological phase transition in two-dimensional square transition-metal dichalcogenides

Yandong Ma,[1,*] Liangzhi Kou,[2] Xiao Li,[3] Ying Dai,[4] Sean C. Smith,[2] and Thomas Heine[1,5,*]

[1]*Department of Physics and Earth Science, Jacobs University Bremen, Campus Ring 1, 28759 Bremen, Germany*

[2]*Integrated Materials Design Centre (IMDC), School of Chemical Engineering, University of New South Wales, Sydney, NSW 2052, Australia*

[3]*Department of Physics, University of Texas at Austin, Austin, Texas 78712, USA*

[4]*School of Physics, Shandong University, 250100 Jinan, People's Republic of China*

[5]*Wilhelm-Ostwald-Institut für Physikalische und Theoretische Chemie, Universität Leipzig, Linnéstrasse 2, 04103 Leipzig, Germany*

(Received 12 June 2015; published 25 August 2015)

Two-dimensional (2D) topological insulators (TIs) hold promise for applications in spintronics based on the fact that the propagation direction of an edge electronic state of a 2D TI is locked to its spin orientation. Here, using first-principles calculations, we predict a family of robust 2D TIs in monolayer square transition-metal dichalcogenides MX_2 (M = Mo, W; X = S, Se, Te), which show sizeable intrinsic nontrivial band gaps ranged from 24 to 187 meV, thus ensuring the quantum spin Hall (QSH) effect at room temperature. Different from the most known 2D TIs with comparable band gaps, these sizeable energy gaps arise from the strong spin-orbit interaction related to d electrons of the Mo/W atoms. A pair of topologically protected helical edge states emerges at the edge of these systems with a Dirac-type dispersion within the bulk band gap. The topologically nontrivial natures are confirmed by the nontrivial Z_2-type topological invariant. More interestingly, with applied strain, a topological quantum phase transition between a QSH phase and a trivial insulating/metallic phase can be realized, and the corresponding topological phase diagram is well established.

DOI: 10.1103/PhysRevB.92.085427 PACS number(s): 73.43.−f, 71.70.Ej, 73.22.−f

I. INTRODUCTION

With the rise in topicality of two-dimensional (2D) materials, hexagonal transition-metal dichalcogenides (TMDCs), with layered structure, have attracted extensive research interest owing to their diverse electronic and magnetic properties [1–4]. They can exhibit semiconducting, metallic, ferromagnetic, and even superconducting behaviors based on the combination of various chalcogens and transition-metal atoms. MX_2(M = Mo,W;X = S,Se,Te) are typical examples of the layered TMDC family. Monolayer MX_2 is a chemically stable 2D material with a honeycomb lattice (labeled as 1H phase – i.e., the monolayer of the ground-state 2H phase of group 6 MX_2), similar to graphene [1,2]. It is composed of three atomic layers, a hexagonal layer of M atoms sandwiched between two hexagonal layers of X atoms. The sandwich monolayer MX_2 is tightly bound internally. Unlike semimetallic graphene, pristine 1H MX_2 monolayers are direct band-gap semiconductors with band-gap values from 1.1 to 1.9 eV [5–9]. Given the facile fabrication, chemical stability, relatively high mobility, and strong spin-orbit coupling (SOC), these materials are expected to have a significant impact on next-generation ultrathin electronic, optoelectronic, and valleytronic devices [10–15]. Besides, monolayer MX_2 can exhibit in other phases displaying many interesting properties. For example, different from the 1H phase, the 1T phase MoS_2 monolayer is metallic.

Following the well-known theoretical discovery of the quantum spin Hall (QSH) effect in the 2D topological insulator (TI) graphene [16], extensive efforts have been devoted to search for new 2D materials or new schemes to realize 2D TIs with large band gaps [17–21]. Interestingly, it was shown recently that monolayers MX_2 become 2D TIs when they are transformed into 1T′ structure [22]. The frontier orbitals of monolayer MX_2 in the low-energy range are dominated by the d orbitals for both the 1H and 1T structure, showing a normal band order and a corresponding trivial topological phase. In contrast, the states around the Fermi level of 1T′ structure have their main contributions from the p and d orbitals. A band inversion between X-p and M-d bands takes place in monolayer MX_2 with 1T′ phase, leading to 2D TIs [22]. In these materials, the spin-filtered edge states exhibit a dissipationless spin or charge transport in the absence of magnetic scatters, offering promising applications in spintronics and quantum computations [23]. Furthermore, a proposal to engineer time-reversal-invariant topological phases in 2D MX_2 under strain and/or in heterostructures that induce superlattice potentials was also reported [24]. Apart from these, recently another monolayer MoS_2 allotrope, which consists of repeated square-octagon rings (labeled as 1S-MX_2), was theoretically found [15,25]. Interestingly, they found that this monolayer possesses both massless Dirac fermions and heavy fermions. However, its topological properties were neglected.

In this work, we report a series of 2D TIs with a sizeable band gap in the square phase of monolayer 1S-MX_2 as predicted by first-principles density-functional calculations. These phases are energetically competitive to the experimentally demonstrated 1T phase and thus can be expected to be prepared experimentally. The calculated Z_2 invariants and edge states provide direct evidence for their nontrivial topology. These new 2D TIs have relatively sizeable band gaps that exceed the thermal energy at room temperature, making possible practical applications at room temperature. Different from TIs in the 1T′ phase where the frontier bands are mainly from the p and d orbitals [22], the frontier orbitals of the

*Corresponding authors: myd1987@gmail.com; t.heine@jacobs-university.de

1S phase are dominated exclusively by the *d* electrons. With an applied strain, the electronic state can experience a significant change. For monolayer MoS_2, $MoSe_2$, $MoTe_2$, WS_2, and WSe_2, there is a topological quantum phase transition between a QSH phase and a trivial insulating or metallic phase under the strain field. For monolayer $MoTe_2$, though the QSH phase can be retained, its topological gap can be turned to a great extent. The strain-induced tunability of the topological phase renders them more attractive for applications in the semiconductor industry.

II. COMPUTATIONAL METHODS

Our calculations are based on density-functional theory (DFT), with the generalized gradient approximations (GGA) [26] of Perdew-Burke-Ernzerhof (PBE) [27] for electron-electron interactions, as implemented in the Vienna *ab initio* simulation pack (VASP) code [28,29]. The projector augmented wave (PAW) method [30,31] is employed in the DFT calculations. The vacuum layer is set to 18 Å to avoid spurious interactions between the MX_2 monolayer and its periodic images. The Brillouin zone integration is performed with a $9\times9\times1k$ mesh for geometry optimization, while a $17\times17\times1k$ mesh is used for self-consistent electronic structure calculations. An energy cutoff of 500 eV is used for the plane-wave expansion of the electronic wave function. Geometries are fully relaxed until the force on each atom is less than 0.01 eV/Å, and the convergence criteria for the total energy is 10^{-6} eV. Phonon dispersion diagrams are obtained by the finite displacement method, as implemented in the CASTEP code [32,33], also employing the PBE functional.

TABLE I. The relative total energies (meV/atom) of the four phases of monolayer MX_2.

	MoS_2	$MoSe_2$	$MoTe_2$	WS_2	WSe_2	WTe_2
1H	0	0	0	0	0	0
1T	280	235	172	296	258	189
1T′	184	110	14	180	90	−29
1S	286	243	183	326	268	181

III. RESULTS AND DISCUSSION

Figure 1(a) shows the typical lattice structure of 1S-MX_2 after geometry relaxation. Similar to the commonly studied monolayer 1H-MX_2, 1S-MX_2 can be also viewed as a three-layer stacking of *M* and *X* atoms, wherein *M* atoms are sandwiched between layers of *X* atoms and each *M* atom is coordinated to six *X* atoms [15,25]. Instead of the six-membered rings in the honeycomb lattice, it is seen that 1S-MX_2 possesses four- and eight-membered rings, motifs that have been found at grain boundaries of 1H-MX_2 [34]. In this configuration, square-octagon pairs are repeated along the *a* and *b* axis, forming a 2D sheet which presents a square Bravais lattice with D_{4h} symmetry and with four *M* and eight *X* atoms per unit cell [marked by the black lines in Fig. 1(a)]. The inversion symmetry exists in this configuration. The equilibrium lattice constants are 6.336, 6.613, 7.055, 6.359, 6.643, and 7.105 Å for 1S-MoS_2, 1S-$MoSe_2$, 1S-$MoTe_2$, 1S-WS_2, 1S-WSe_2, and 1S-WTe_2, respectively. The relative total energies of the four phases of monolayer MX_2 are given in Table I. We can see that, for all the systems studied here, the total energies of the 1S phases are comparable to that of

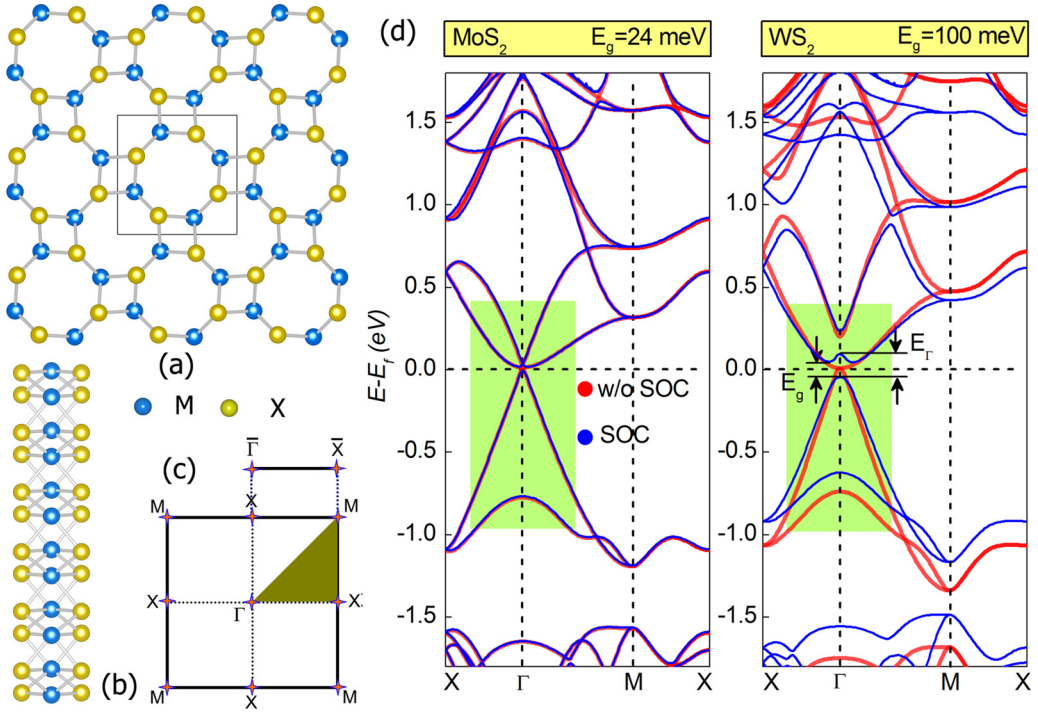

FIG. 1. (Color online) Crystal structures of monolayer 1S-MX_2 from (a) top and (b) side views. (c) 2D Brillouin zone of monolayer 1S-MX_2 and one-dimensional (1D) projected Brillouin zone of the corresponding nanoribbon with high-symmetry points. (d) Band structures of monolayer 1S-MoS_2 and 1S-WS_2 with and without SOC. The Fermi level is set to zero.

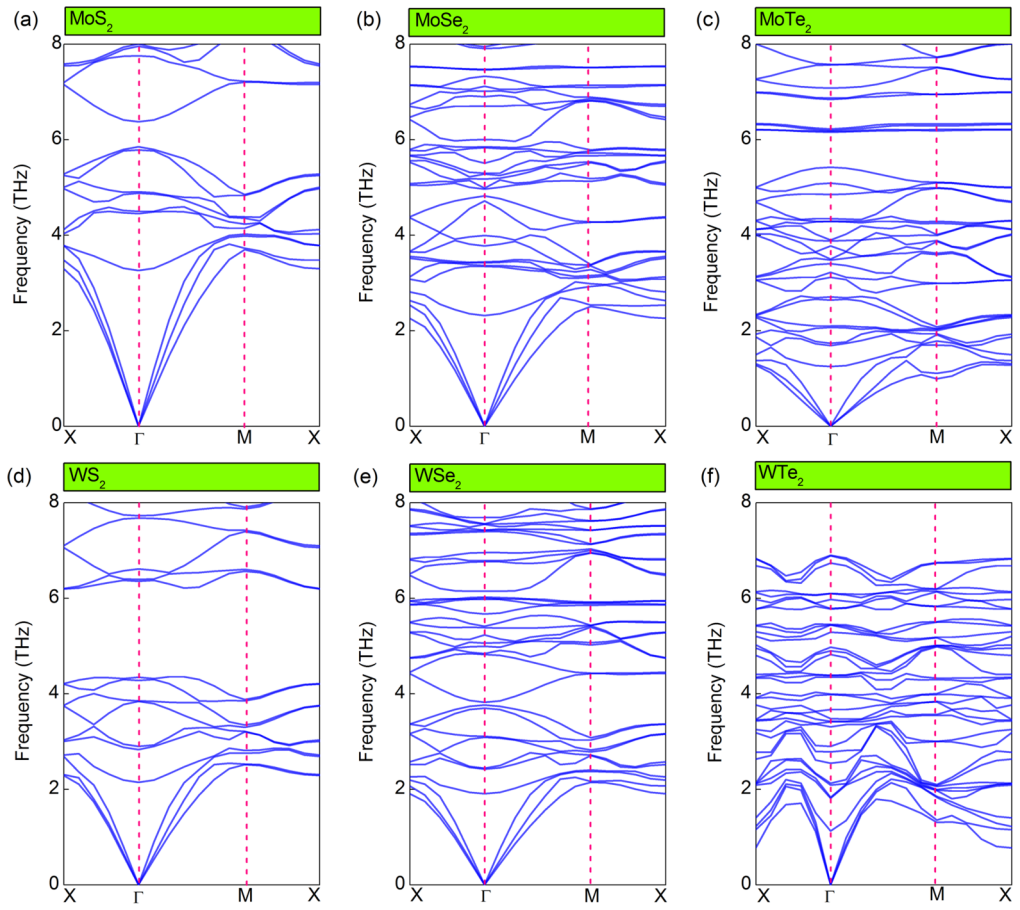

FIG. 2. (Color online) Phonon band dispersion of (a) 1S-MoS_2, (b) 1S-$MoSe_2$, (c) 1S-$MoTe_2$, (d) 1S-WS_2, (e) 1S-WSe_2, and (f) 1S-WTe_2.

the corresponding 1T phases [35,36]. Considering the fact that the 1T phase has been observed in some samples [37] and material synthesis of monolayer MX_2 are rapidly developing, we believe that our work will stimulate immediate interest in experimental synthesis of the 1S phase and that these systems can be realized in experimentation soon. In Fig. 2 we present the calculated phonon dispersion of 1S-MX_2. The frequencies of all phonon branches in the whole Brillouin zone have positive values, showing that these compounds are stable, corresponding to an energy minimum in the potential energy landscape.

The band structures of 1S-MoS_2 and 1S-WS_2, as representatives of the band structures of 1S-MX_2, are shown in Fig. 1(d), and the zoom-in of the corresponding bands near the Γ point around the Fermi level are depicted with orbital projections in Fig. 3(a). The band structures of other monolayers are provided in the Supplemental Material [38]. Without considering SOC, the valence band maximum (VBM) and conduction band minimum (CBM) of all these monolayers touch at the Γ point, with the Fermi level exactly across the touching points, and these monolayers can be regarded as gapless semiconductors. Although they share the same composition, the electronic characters of 1S-MX_2 are in stark contrast to those of monolayers 1H-MX_2, which are semiconductors with a direct band gap at the K point. Based on the orbital-resolved band structures of 1S-MoS_2 and 1S-WS_2 in Fig. 3(a), the highest valence band and lowest conduction band (HVB and LCB) of 1S-MX_2 are mainly contributed by the $d_{x^2-y^2}$ (blue) and d_z^2 (red) orbitals of the M atoms, respectively, with negligible contributions from the p orbitals of the X atoms. For 1S-MoS_2, the second lowest conduction band (labeled as LCB + 1) at the Γ point is very close to the touching point of VBM and CBM, which reside 3 meV above this point. To give a deeper insight into the dispersion relation of 1S-MoS_2 around the touching point, the corresponding bands around the Fermi level are presented in two-dimensional k space, as shown in Fig. 3(b). It is seen that HVB and LCB indeed touch at the Fermi level. Unlike the case of 1S-MoS_2, the LCB + 1 is well separated from the touching points for the other five 1S-MX_2 monolayers studied here (see Fig. 1(d) and Supplemental Material [38]).

SOC is responsible for opening a gap at the touching points, that means those 1S-MX_2 monolayers have strong spin-orbit couplings and are insulating (see Fig. 1(d) and Supplemental Material [38]). The orbital-resolved band structure with SOC in Fig. 3(a) reveals that the HVB at the Γ point of 1S-MoS_2 is contributed by d_{x2-y2} and d_{z2} orbitals, while LCB at the Γ point is mainly from d_{x2-y2} orbitals. In contrast, for the electronic states of 1S-MoS_2 without considering SOC and the other five monolayers with/without SOC, both the HVB and LCB at the Γ point are dominated by both d_{x2-y2} and d_{z2}. The difference can be well understood by looking at the remainder of the band structures of 1S-MoS_2 without SOC: compared with the other monolayers, where LCB + 1 is well separated from

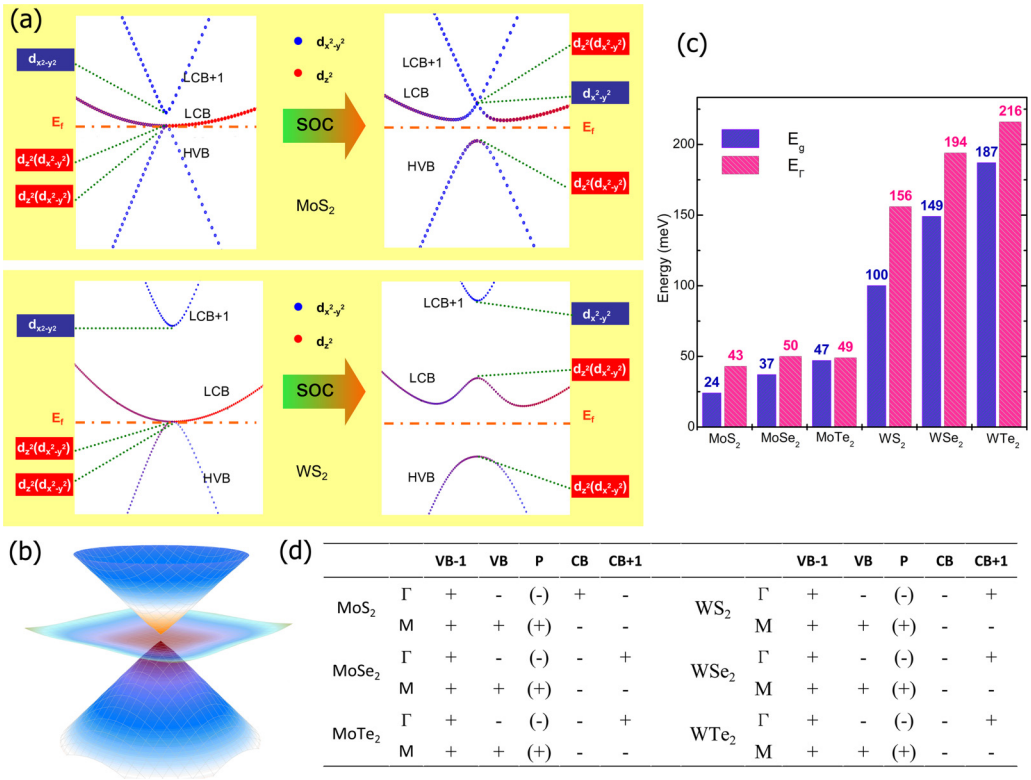

(d)

		VB-1	VB	P	CB	CB+1			VB-1	VB	P	CB	CB+1
MoS_2	Γ	+	-	(-)	+	-	WS_2	Γ	+	-	(-)	-	+
	M	+	+	(+)	-	-		M	+	+	(+)	-	-
$MoSe_2$	Γ	+	-	(-)	-	+	WSe_2	Γ	+	-	(-)	-	+
	M	+	+	(+)	-	-		M	+	+	(+)	-	-
$MoTe_2$	Γ	+	-	(-)	-	+	WTe_2	Γ	+	-	(-)	-	+
	M	+	+	(+)	-	-		M	+	+	(+)	-	-

FIG. 3. (Color online) (a) The evolution of orbital-resolved band structures of 1S-MoS_2 and 1S-WS_2 when taking into account SOC. (b) Band structure of 1S-MoS_2 around the Fermi level in 2D k space with energy as the third dimension. (c) The global band gap (E_g) and the SOC-induced direct band gap at the Γ point (E_Γ) of 1S-MX_2. (d) The parities of HVB-1, HVB, LCB, and LCB + 1 at the Γ and M points for 1S-MX_2; the products of the occupied bands at the Γ and M points are also listed in the brackets. $\delta(X)^2 \equiv 1$ has no effect on band topology, and therefore the results at the X points are not shown here.

LCB without SOC, the LCB + 1 of 1S-MoS_2 is located only 3 meV above the touching point at the Γ point. Besides, it is noted that the LCB + 1 at the Γ point is mainly contributed by d_{x2-y2} orbitals. Therefore, SOC imposes a band exchange between LCB and LCB + 1 at the Γ point for 1S-MoS_2. For the other monolayers, such a band exchange has not been observed. We define the energy splitting at the Γ point between the aforementioned valence band (HVB) and the conduction bands (LCB or LCB + 1) composed of both d_{x2-y2} and d_{z2} orbitals as a SOC-induced direct band gap, E_Γ. As shown in Fig. 3(c), the E_Γ are in the range of 43–216 meV. E_Γ of 1S-WX_2 is significantly larger than that of the corresponding 1S-MoX_2, demonstrating a stronger SOC for the heavier W atoms compared with the Mo atoms. Because of the Mexican-hat shape of LCB in the presence of SOC, the global band gaps, E_g, of these 1S-MX_2 monolayers are different from their E_Γ, ranging from 24 to 187 meV. Especially for the 1S-WX_2 monolayer, the nontrivial global band gaps are all more than 100 meV, which far exceeds the thermal energy at room temperature. Such sizeable band gaps of 1S-MX_2, arising from the strong SOC of the d electrons of the M atoms, will survive against the thermal fluctuation at room temperature or even higher temperature.

To characterize the topological nature of the insulating phase of 1S-MX_2, we calculate the Z_2 topological invariants within the DFT frame. In two dimensions, the band topology is determined by one Z_2 topological invariant (ν), where $\nu = 1$ corresponds to a topologically nontrivial phase and $\nu = 0$ to a topologically trivial phase. Due to the presence of inversion symmetry in the 1S-MX_2 monolayers, the topological invariant ν can be directly computed based on the parity of the wave function of occupied energy bands at the time-reversal-invariant momenta (TRIM) [39]. As shown in Fig. 1(c), there are four TRIM for 1S-MX_2, located at Γ point, one M point, and two X points, where M is the vertex and X are the midpoints of the sides of the square Brillouin zone. ν is obtained by the relations

$$\delta(K_i) = \prod_{m=1}^{N} \xi_{2m}^{i}, \quad (-1)^{\nu} = \prod_{i=1}^{4} \delta(K_i) = \delta(\Gamma)\delta(M)\delta(X)^2.$$

Here, $\delta(K_i)$ is the product of parity eigenvalues at the TRIM, $\xi = \pm 1$ is the parity eigenvalue of the wave function, and N is the total number of degenerate occupied bands. The results of the band topology are listed in Fig. 3(d). It is found that 1S-MX_2 monolayers are nontrivial 2D TIs with Z_2-type topological invariant $\nu = 1$. Considering their sizable nontrivial band gaps, the QSH effect can be readily realized at room temperature. By closely examining the parities of the low-energy bands, it is seen that if SOC is switched off, the two degenerate states (apart from the spin degeneracy) at the touching point both have odd parities. SOC lifts this degeneracy with unchanged parities. In this process, there is no parity exchange between the valence and conduction bands.

Therefore, SOC does not induce any band inversion between the valence and conduction bands at the TRIM in 1S-MX_2. The only effect of SOC is to break the degeneracy at the touching point and to open an insulating gap. This is different from some well-known TIs, such as Bi_2Se_3, where the SOC is responsible for the band inversion. Such characteristics of "intrinsic nontrivial band order" have been recently found in several other systems, such as the chemically modified Bi and Sn honeycomb lattices [17,18,21]. The underlying mechanism of the "intrinsic nontrivial band order" in 1S-MX_2 is similar to the situation in graphene and chemically modified Bi and Sn honeycomb lattices [17,18,21], which results from the Van Hove singularity [40]. In 2D systems, a saddle point occurs where the curvature of the bands has opposite sign in two different directions, leading to a Van Hove singularity. The crossing of one band with Van Hove singularity with another one can lead to a nontrivial band order, even without including SOC. For 1S-MX_2 without SOC, the degeneracy at the Fermi level can be considered as an overlap of saddle points from two bands with Van Hove singularity. With this in mind, we can understand why 1S-MX_2 has nontrivial band order even before SOC is included.

The 2D nontrivial insulating state is characterized by topologically protected conducting edge states within the bulk gap. To confirm the existence of the topological edge states, we construct a nanoribbon of 1S-MX_2 monolayer, with all the dangling bonds passivated by hydrogen atoms [41]. To minimize the interaction between two edges of the nanoribbon, we adopt an 11-unit-cell-thick nanoribbon for 1S-MX_2 with the width of over 6.7 nm. The calculated band structures of 1S-MoS_2 and 1S-WS_2 nanoribbons are shown in Fig. 4, while the corresponding results for the other systems are shown in the Supplemental Material [38]. The bands in Fig. 4 are all twofold degenerate, due to the simultaneous presence of the time reversal symmetry and inversion symmetry in our nanostructure. Within the bulk band gap there is a pair of gapless degenerate bands crossing at the $\bar{\Gamma}$ point (red color lines), which are edge states because they are localized at the edges of the nanoribbon. Such edge states confirm the nontrivial topology of the 1S-MX_2 monolayer. It is noted that there are other states very close to edge bands, which have wide spatial distribution and thus bulk state characteristics, in stark contrast to edge states.

For actual conditions, one critical concern is the effect of boundary on the topological edge states. That is because, as in the situation of 1T phase [37], probably the 1S phase would appear coexisting with the regular 1H phase. Then it would be important to investigate what happens with the topological edge states at the boundaries between the 1S and 1H phases. On one hand, the nontrivial edge states can still appear in the bulk band gap and be not affected by such a boundary. On the other hand, the trivial edge states may appear in the band gap and then hybridize with the nontrivial edge states [42], which thus may affect their topological performances. Besides the boundary, various defects, which usually present in 2D materials during their growth, may also affect the topological properties. To this end, a more comprehensive study concerning these factors should be performed in further works.

Based on the calculations of the band topology and edge states above, we have demonstrated the nontrivial topology

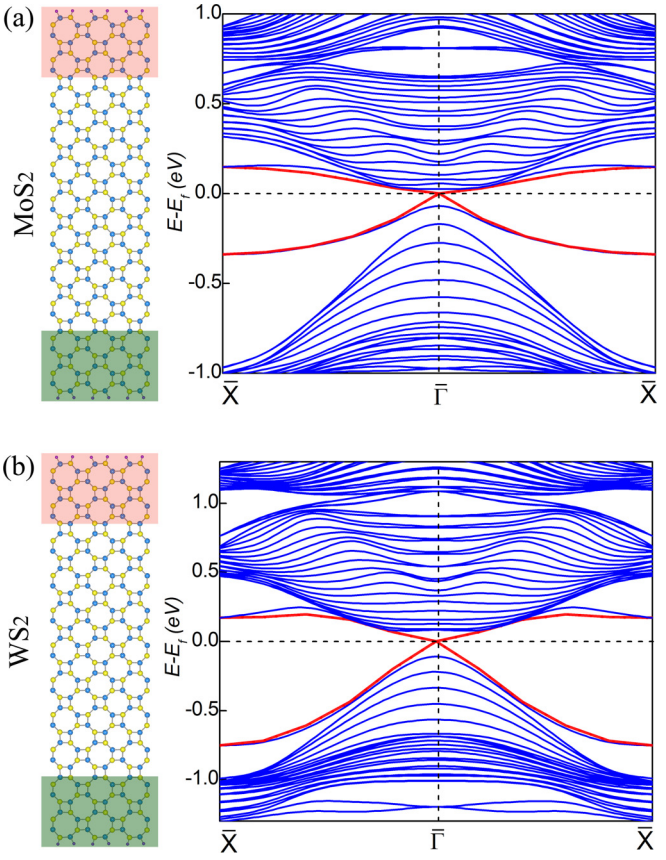

FIG. 4. (Color online) Atomic and band structures of (a) 1S-MoS_2 and (b) 1S-WS_2 nanoribbons. The red lines denote electronic states localized on edge atoms, while blue ones denote nonlocalized states. The Fermi level is set to zero.

with sizable band gaps in 1S-MX_2 monolayers. For the purpose of technological applications, it is of particular interest to further investigate the strain effect on the topological properties. The applied strain can modify the electronic properties in diverse materials [43–49], such as strain-engineered band gaps in 1H-MoS_2 monolayer [49]. Therefore, the strain field is expected to tune the magnitude of the band gap of our 1S-MX_2 systems as well, and even change their band topology in a controllable manner, which, if possible, will have potential use in TI-based electronics. In the following, we calculate the electronic structures of 1S-MX_2 monoalyers under the biaxial strain to examine the tunability of the nontrivial band gap and the possible existence of a topological phase transition. The biaxial strain field is constructed by isotropically increasing the lattice constants. For each fixed lattice constant, the atomic positions are fully reoptimized. The magnitude of the strain is defined by $\varepsilon = (a - a_0)/a_0$, where a_0 and a are the lattice constants of the unstrained and strained 1S-MX_2 monolayers, respectively.

In Fig. 5 and its inset, we show the band gap and the topological phase diagram of 1S-MX_2 as a function of strain. The corresponding band structures of 1S-MX_2 under strain are shown in the Supplemental Material [38]. It is seen that both the band gap and the topological phase are indeed sensitive to the applied strain and a topological phase transition can be

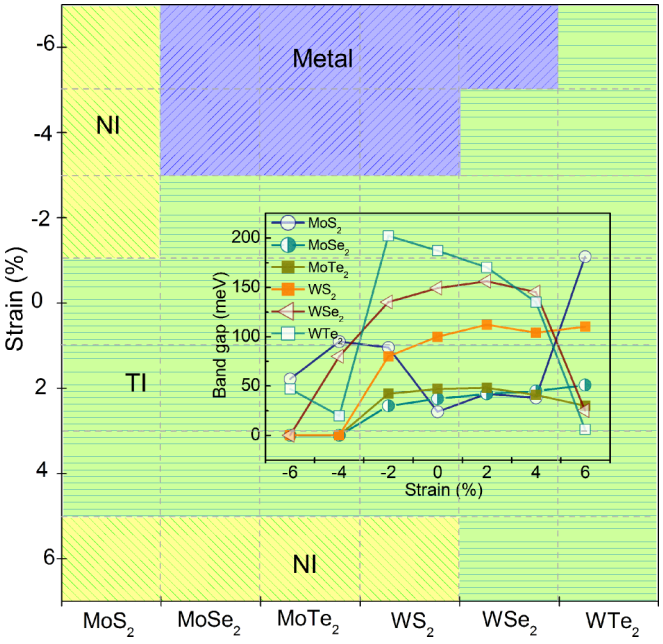

FIG. 5. (Color online) Topological phase diagram of 1S-MX_2 as a function of strain. The insert shows the value of the global band gap (E_g) of 1S-MX_2 as a function of strain.

induced in most 1S-MX_2 monolayers. We find that 1S-MoS_2 is located very close to the phase boundary between the QSH phase and a trivial insulating phase. Within a strain range from 0% to 4%, 1S-MoS_2 is in the QSH phase, which is identified by the well-defined nontrivial Z_2-type topological invariant. When the lattice is expanded by 6% or compressed by more than −2%, 1S-MoS_2 would transform into a trivial insulating phase, leading to a topological phase transition in 1S-MoS_2. For 1S-$MoSe_2$, 1S-$MoTe_2$, and 1S-WS_2, there is a relatively slow response of the band topology to the compressive strain compared with 1S-MoS_2. The compressive strain reaches up to −2% without changing the band topology in these three monolayers. When the compressive strain reaches −4%, a topological phase transition takes place, and they transform into a metallic phase with the hole and electron pockets at different k points, while the topological transition under 6% extensive strain lead to a the trivial insulating phase. Therefore, with increasing strain from −6% to 6%, 1S-$MoSe_2$, 1S-$MoTe_2$, and 1S-WS_2 undergo a metallic phase → nontrivial topological phase → trivial insulating phase in sequence. For 1S-WSe_2, the nontrivial topological insulator property is stable in a larger strain range until the strain reaches −6%, where 1S-WSe_2 is changed into the metallic phase, and no trivial insulating phase can be obtained in 1S-WSe_2 within the calculated strain range. This significant strain dependence demonstrates that the nontrivial topological properties in these systems can be effectively tuned. Therefore, it will be very interesting to achieve strain-induced topological phase transitions in these systems in experiments which will have potential use in electronics and spintronics. On the other hand, the nontrivial topological phase of 1S-WTe_2 survives in the strain range from −6% to 6%, indicating its robust stability against mechanical deformation. This makes the QSH effect in 1S-WTe_2 highly adaptable in various strain environments. Moreover, the comprehensive phase diagrams provide a guide in the search for viable substrates for growing or supporting these monolayers to realize the nontrivial topology and topological phase transitions in 2D-TI systems.

IV. CONCLUSION

In conclusion, first-principles density-functional calculations have been performed to study the electronic and topological properties of 1S-MX_2 monolayers, an energetically competitive phase of group-6 MX_2 2D materials. All the monolayers studied here are predicted to be promising 2D TIs with nontrivial Z_2-type topological invariants and a pair of topologically protected helical edge states at the edge of the nanoribbon. These 2D TIs have sizable bulk band gaps ranging from 24 to 187 meV, which far exceed the thermal energy and ensure the QSH effect at room temperature. Interestingly, a topological quantum phase transition between the QSH phase and a trivial insulating/metallic phase can take place in 1S-MX_2 under an external strain, which offers a feasible approach to band engineering in a controllable way. 1S-MX_2 monolayers, with a sizeable and tunable topological band gap, will provide a platform for diverse potential applications.

Note added. We noticed two similar works [50,51] on the prediction of 1S-MX_2 monolayers as 2D TIs which were submitted to arXiv at almost the same time as ours.

ACKNOWLEDGMENTS

Financial support from the European Research Council (ERC, StG 256962) and the National Science Foundation of China under Grant No. 11174180 are gratefully acknowledged.

[1] J. N. Coleman, M. Lotya, A. O'Neill, S. D. Bergin, P. J. King, U. Khan, K. Young, A. Gaucher, S. De, R. J. Smith, I. V. Shvets, S. K. Arora, G. Stanton, H. Y. Kim, K. Lee, G. T. Kim, G. S. Duesberg, T. Hallam, J. J. Boland, J. J. Wang, J. F. Donegan, J. C. Grunlan, G. Moriarty, A. Shmeliov, R. J. Nicholls, J. M. Perkin, E. M. Grieveson, K. Theuwissen, D. W. McComb, P. D. Nellist, and V. Nicolosi, Science **331**, 568 (2011).

[2] K. S. Novoselov, D. Jiang, F. Schedin, T. Booth, V. V. Khotkevich, S. V. Morozov, and A. K. Geim, Proc. Natl. Acad. Sci. USA **102**, 10451 (2005).

[3] Y. D. Ma, Y. Dai, M. Guo, C. W. Niu, Y. T. Zhu, and B. B. Huang, ACS Nano **6**, 1695 (2012).

[4] W. Liu, J. Kang, D. Sarkar, Y. Khatami, D. Jena, and K. Banerjee, Nano Lett. **13**, 1983 (2013).

[5] K. F. Mak, C. Lee, J. Hone, J. Shan, and T. F. Heinz, Phys. Rev. Lett. **105**, 136805 (2010).

[6] A. Kuc, N. Zibouche, and T. Heine, Phys. Rev. B **83**, 245213 (2011).

[7] Y. D. Ma, Y. Dai, M. Guo, C. N. Niu, J. B. Lu, and B. B. Huang, Phys. Chem. Chem. Phys. **13**, 15546 (2011).

[8] A. Kumar and P. K. Ahluwalia, Eur. Phys. J. B **85**, 186 (2012).
[9] C. Ataca, H. Şahin, and S. Ciraci, J. Phys. Chem. C **116**, 8983 (2012).
[10] B. Radisavljevic, A. Radenovic, J. Brivio, V. Giacometti, and A. Kis, Nat. Nanotechnol. **6**, 147 (2011).
[11] Y.-J. Zhang, J.-T. Ye, Y. Matsuhashi, and Y. Iwasa, Nano Lett. **12**, 1136 (2012).
[12] D. Xiao, G.-B. Liu, W. Feng, X. Xu, and W. Yao, Phys. Rev. Lett. **108**, 196802 (2012).
[13] N. F. Q. Yuan, K. F. Mak, and K. T. Law, Phys. Rev. Lett. **113**, 097001 (2014).
[14] Z. Y. Zhu, Y. C. Cheng, and U. Schwingenschlögl, Phys. Rev. B **84**, 153402 (2011).
[15] W. Li, M. Guo, G. Zhang, and Y.-W. Zhang, Phys. Rev. B **89**, 205402 (2014).
[16] C. L. Kane and E. J. Mele, Phys. Rev. Lett. **95**, 226801 (2005).
[17] Y. Xu, B. H. Yan, H.-J. Zhang, J. Wang, G. Xu, P. Tang, W. H. Duan, and S.-C. Zhang, Phys. Rev. Lett. **111**, 136804 (2013).
[18] Z. G. Song, C. C. Liu, J. B. Yang, J. Z. Han, B. T. Fu, M. Ye, Y. C. Yang, Q. Niu, J. Lu, and Y. G. Yao, NPG Asia Mater. **6**, e147 (2014).
[19] F.-C. Chuang, L.-Z. Yao, Z.-Q. Huang, Y.-T. Liu, C.-H. Hsu, T. Das, H. Lin, and A. Bansil, Nano Lett. **14**, 2505 (2014).
[20] H. Weng, X. Dai, and Z. Fang, Phys. Rev. X **4**, 011002 (2014).
[21] Y. D. Ma, Y. Dai, L. Z. Kou, T. Frauenheim, and T. Heine, Nano Lett. **15**, 1083 (2015).
[22] X. F. Qian, J. W. Liu, L. Fu, and J. Li, Science **346**, 1344 (2014).
[23] A. Roth, C. Brune, H. Buhmann, L. W. Molenkamp, J. Maciejko, X.-L. Qi, and S.-C. Zhang, Science **325**, 294 (2009).
[24] M. A. Cazalilla, H. Ochoa, and F. Guinea, Phys. Rev. Lett. **113**, 077201 (2014).
[25] H. Terrones and M. Terrones, 2D Mater. **1**, 011003 (2014).
[26] J. P. Perdew and Y. Wang, Phys. Rev. B **45**, 13244 (1992).
[27] J. P. Perdew, K. Burke, and M. Ernzerhof, Phys. Rev. Lett. **77**, 3865 (1996).
[28] G. Kresse and J. Furthmüller, Comput. Mater. Sci. **6**, 15 (1996).
[29] G. Kresse and J. Furthmüller, Phys. Rev. B **54**, 11169 (1996).
[30] P. E. Blöchl, Phys. Rev. B **50**, 17953 (1994).
[31] G. Kresse and D. Joubert, Phys. Rev. B **59**, 1758 (1999).
[32] S. J. Clark, M. D. Segall, C. J. Pickard, P. J. Hasnip, M. I. J. Probert, K. Refson, and M. C. Payne, Z. Kristallogr. **220**, 567 (2005).
[33] K. Refson, P. R. Tulip, and S. J. Clark, Phys. Rev. B **73**, 155114 (2006).
[34] A. M. van der Zande, P. Y. Huang, D. A. Chenet, T. C. Berkelbach, Y. You, G.-H. Lee, T. F. Heinz, D. R. Reichman, D. A. Muller, and J. C. Hone, Nat. Mater. **12**, 554 (2013).
[35] D. Voiry, M. Salehi, R. Silva, T. Fujita, M. Chen, T. Asefa, V. B. Shenoy, C. Eda, and M. Chhowalla, Nano Lett. **13**, 6222 (2013).
[36] B. Mahler, V. Hoepfner, K. Liao, and G. A. Ozin, J. Am. Chem. Soc. **136**, 14121 (2014).
[37] G. Eda, T. Fujita, H. Yamaguchi, D. Voiry, M. W. Chen, and M. Chhowalla, ACS Nano **6**, 7311 (2012).
[38] See Supplemental Material at http://link.aps.org/supplemental/10.1103/PhysRevB.92.085427 for detailed information about the electronic band structures for 1S-MX_2, band structures of 1S-MX_2 ribbons, and band structures of 1S-MX_2 under different strains. This material is available free of charge via the Internet.
[39] L. Fu, C. L. Kane, and E. J. Mele, Phys. Rev. Lett. **98**, 106803 (2007).
[40] L. Van Hove, Phys. Rev. **89**, 1189 (1953).
[41] X. Li, H. W. Liu, H. Jiang, F. Wang, and J. Feng, Phys. Rev. B **90**, 165412 (2014).
[42] R.-L. Chu, G.-B. Liu, W. Yao, X. D. Xu, D. Xiao, and C. W. Zhang, Phys. Rev. B **89**, 155317 (2014).
[43] C. Si, J. W. Liu, Y. Xu, J. Wu, B.-L. Gu, and W. H. Duan, Phys. Rev. B **89**, 115429 (2014).
[44] C.-C. Liu, W. X. Feng, and Y. G. Yao, Phys. Rev. Lett. **107**, 076802 (2011).
[45] J. W. Liu, X. F. Qian, and L. Fu, Nano Lett. **15**, 2657 (2015).
[46] J. J. Zhou, W. X. Feng, C.-C. Liu, S. Guan, and Y. G. Yao, Nano Lett. **14**, 4767 (2014).
[47] W. Luo and H. J. Xiang, Nano Lett. **15**, 3230 (2015).
[48] Y. F. Ge, W. H. Wan, W. X. Feng, D. Xiao, and Y. G. Yao, Phys. Rev. B **90**, 035414 (2014).
[49] J. Feng, X. F. Qian, C.-W. Huang, and J. Li, Nat. Photon. **6**, 866 (2013).
[50] Y. Sun, C. Felser, and B. H. Yan, arXiv:1503.08460.
[51] S. M. Nie, Z. D. Song, H. M. Weng, and Z. Fang, Phys. Rev. B **91**, 235434 (2015).